In the hundreds of bands of the photographed substance, hyperspectral imaging delivers a great density of spectral data. This allows the images to be used for a variety of purposes, including agriculture, geosciences, and biomedical imaging. Previous work didn't discuss the best classifier with sufficient ground truth classes. This work presents the application of maximum abundance classification (MAC) for classifying a variety of areas over hyperspectral images. The allocation of an end-member throughout hyperspectral images can be described with abundance maps. Since each pixel's abundance values represent the proportion of each end-member that is present in that pixel, the pixels in a hyperspectral image will be classified in this study by determining the highest abundance rate of every pixel and allocating it to the corresponding end-member category. The ground truth classes are represented by nine end-members in the test data: Bitumen, Shadows, Self-Blocking Bricks, Bare Soil, highlighted Metal area, Gravel, Meadows, Trees, and Asphalt. By uniformly distributing the range of wavelength over the amount of spectral domains, we initially determine the central wavelength for each band to visualize loaded data and the end-member signatures of nine ground truth classes. Next, we estimate the end-members abundance maps. Finally, we classify the Max Abundance of every pixel to present a color-coded image, the overlaid, and the classified hyperspectral image areas over their category labels. The result demonstrates that brick, bare soil, trees, and asphalt zones have all been correctly identified in the photographs, which is beneficial for the identification or detection of materials

Keywords: hyperspectral image processing, maximum abundance classifier, ground truth, satellite maps

UDC 621
DOI: 10.15587/1729-4061.2023.271774

DEVELOPING SATELLITE HYPERSPECTRAL IMAGE PROCESSING USING A MAXIMUM ABUNDANCE CLASSIFIER WITH NINE GROUND TRUTH CLASSES

Ghassan Ahmad Ismaeel
Corresponding author
Master of Computer Engineering
Department of Clinical Laboratory Sciences
College of Pharmacy
University of Mosul
Al-Majmoaa str., Mosul, Iraq, 41002
Mina Basheer Gheni
Master of Computer Science
Department of Computer
Al-Nahrain University
Al Jadriyah Bridge, Baghdad, Iraq, 64074
Saad Qasim Abbas
Master in Medical Instrument Engineering
Department of Medical Instrument Engineering Technique
Al-Turath University College
Al Mansour, Baghdad, Iraq, 10068
Mustafa Musa Jaber
PhD, Lecturer
Department of Medical Instruments Engineering Techniques
Dijlah University College
Al-Dora str., 100, Baghdad, Iraq, 10021
Mohammed Hasan Ali
PhD, Lecturer
Department of Computer Systems and Software Engineering
Imam Ja'afar Al-Sadiq University
Baghdad H.w., Najaf, Iraq, 16012

Received date 10.10.2022
Accepted date 10.01.2023
Published date 28.02.2023

***How to Cite**: Ismaeel, G. A., Gheni, M. B., Abbas, S. Q., Jaber, M. M., Ali, M. H. (2023). Developing satellite hyperspectral image processing using a maximum abundance classifier with nine ground truth classes. Eastern-European Journal of Enterprise Technologies, 1 (2 (121)), 14–20. doi: https://doi.org/10.15587/1729-4061.2023.271774*

1. Introduction

Hyperspectral imaging provides a data cube by using a hyperspectral camera. This data can be represented by a book. Red, green, and blue are the three colors that digital or mobile phone cameras use to capture the target, replicating human vision [1]. These hues which are actually wide wavelength channels are equivalent to the amount of data that is being collected. Tens to hundreds of wavelength-specific narrow color channels are used to record the target. It is essential to specify the number of wavelengths that are employed according to the sort of considered hyperspectral camera during covering the whole target region, where the target is traced in 220 wavelengths [2]. This is the amount of data that each wavelength of the hyperspectral image will contain and is displayed as a layer of cubic data. This cubic data provides a great deal of specific information about the target, much of it comes from wavelengths that are invisible to the human eye [3]. In the hundreds of bands of the photographed substance, hyperspectral imaging delivers a great density of spectral data [4, 5]. The majority of contemporary hyperspectral sensors also have a high spatial resolution, allowing the images to be used for a variety of purposes, including agriculture, geosciences, biomedical imaging, molecular biology, astronomy, and surveillance.

Therefore, research and further analysis on the development of processing the hyperspectral images to determine the proportion of material or end-member contributions in each pixel, making it beneficial for the identification or detection of materials are relevant.

2. Literature review and problem statement

The data is acquired via aerial devices like satellites, which can collect massive volumes of data and transfer it to ground stations for processing. In the study [6], an FPGA for the

limited L1/2 NMF (L1/2-NMF) algorithm was devised and implemented on Altera Family FPGAs. However, no specific outcomes have been published. The noise condition of the HJ-1A hyperspectral pictures was analyzed using a method known as residual local standard deviations. In [7], they analyzed the noise state of the HJ-1A hyperspectral images by using the graduated standard deviation method. They also suggested a way to reduce the dimensions of the HJ-1A images, by converting Maximum Break Noise (OMNF). However, they did not touch upon the nine categories of earthly truth. The research [8] dealt with the encoding of the spectral-spatial properties of hyperspectral photo categorization in the internet of things satellite system, but their experimental results showed up only on three HSI datasets. The research [9] examined a deep learning matrix approach to classify hyperspectral satellite images, propose an Initiation-Inspired Architecture (IIA) and combine it with existing HybridSN architectures. However, the results provided a significant decrease in the development of image processing. The paper [10] describes a system for transmitting hyperspectral satellite pictures through wireless channels. A low-complexity Karhunen-Loève 1D transformation (KLT) employing a spectral patterning relationship aggregation technique was developed using the suggested scheme. Although this method has the potential to improve image quality, it cannot process large-resolution images. The hyperspectral satellite images were used to detect the effects of hydrocarbon pollution in the Amazon forests through the interest of the study [11], where the vegetation cover indicators were applied to the hyperspectral Hyperion satellite images. However, their method using hyperspectral satellite imagery did not contribute to the development of hyperspectral satellite image processing. The study [12] was concerned with comparing hyperspectral images and satellite images to detect the concentration of chlorophyll in coastal areas, through the traditional satellite image. Their method of comparing hyperspectral and satellite imagery did not provide insight into its development. As a result, they did not touch upon the use of the Maximum Abundance Classifier with the Nine Classes of Earthly Truth.

It is therefore important to know the strategy that achieves the best way to develop hyperspectral satellite image processing, which is important in a variety of our daily demands. As a result, it is necessary to develop satellite hyperspectral image processing with an effective classifier of sufficient ground truth classes.

3. The aim and objectives of the study

The aim of the study is to develop satellite hyperspectral image processing using a maximum abundance classifier with nine ground truth classes for classifying a variety of areas over hyperspectral images. This will make hyperspectral imaging possible to deliver a great density of spectral data and allows the images to be used for a variety of purposes, including agriculture, geosciences, biomedical imaging, molecular biology, astronomy, and surveillance.

To achieve this aim, the following objectives are accomplished:

– to identify the names of classes of every end-member with its associated column for the signatures matrix and visualize their profiles;

– to generate abundance maps of the end-members using the full constrained least squares (FRLS) method;

– to apply the maximum abundance classifier and show its pixels classified color-coded image.

4. Materials and methods

4. 1. Object and hypothesis of the study

The object of this work is to present an application of maximum abundance classification (MAC) for classifying a variety of areas over hyperspectral images. The allocation of an end-member throughout hyperspectral images can be described with abundance maps. The distribution of an end-member throughout a hyperspectral image is described by an abundance map. There are two types of pixels in the image: pure pixels and mixed pixels. Each pixel's abundance values represent the proportion of each end-member that is present in that pixel.

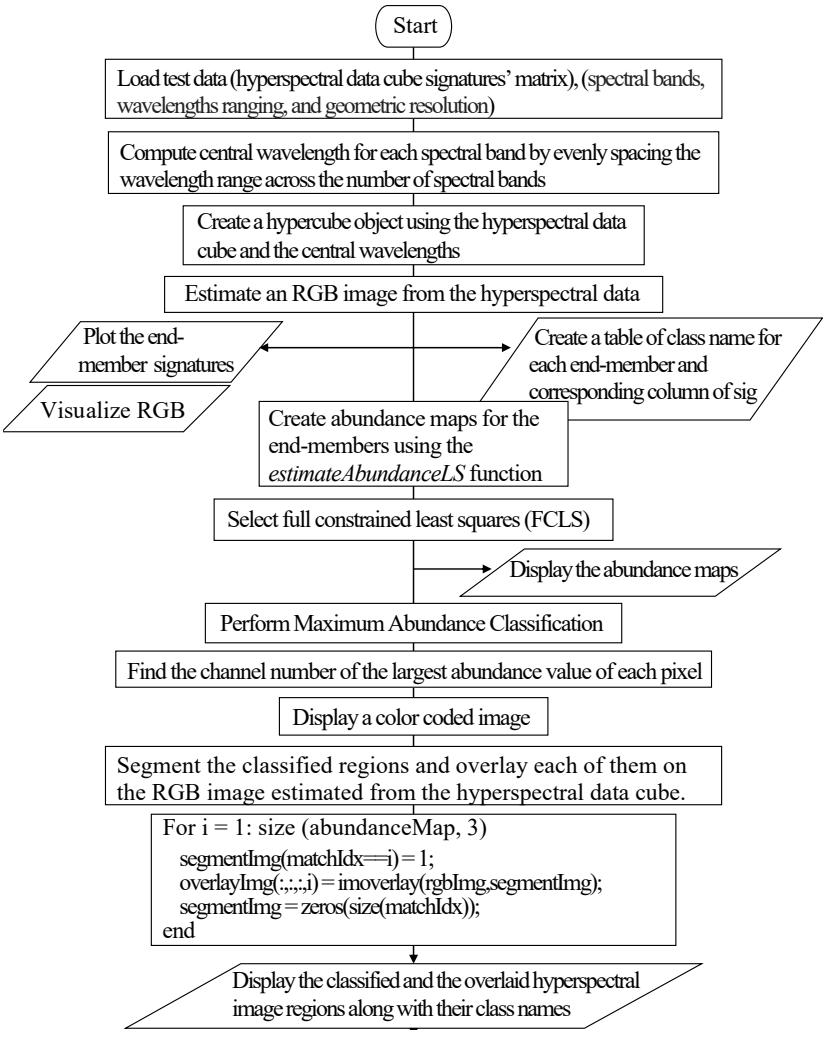

Fig. 1. Flowchart of the methodology steps

By determining each pixel's greatest abundance value and designating it to the corresponding end-member class, we will categorize the pixels in this work's hyperspectral images. MATLAB-based functions are employed to perform the proposed approach that is limited to the use of ground truth classes with nine end-members in the test data including Bitumen, Shadows, Self-Blocking Bricks, Bare Soil, highlighted Metal area, Gravel, Meadows, Trees, and Asphalt.

4. 2. Dataset

This work adopts testing a dataset from Pavia University, which includes ground truth classes represented by nine end-members in the test data: Bitumen, Shadows, Self-Blocking Bricks, Bare Soil, highlighted Metal area, Gravel, Meadows, Trees, and Asphalt.

4. 3. Loading and Visualizing Data

The considered loaded data includes an array (paviaU) [13, 14], which represents the hyperspectral cubic data, signatures' matrix for nine end-members obtained from the hyperspectral data. This cubic data has wavelengths of ranges between 430 nm to 860 nm, 103 spectral bands, a spatial resolution for every band image of 610-to-340, and a numerical resolution of 1.3 m.

Therefore, the loading and visualizing dataset include:

1) computing the center wavelength for each spectral band;

2) creating a hypercube object;

3) plotting the end-member signatures.

In this stage, the central wavelengths are calculated for every spectral band by evenly distributing the range of wavelengths over several spectral bands. Next, a hypercube object is generated by central wavelengths and the hyperspectral cubic data. Then an RGB image for hyperspectral cubic data is estimated. Then the parameter value of the contrast stretching is set to true for improving the obtained RGB contrast.

4. 4. Estimating Abundance Maps

Utilize the *estimateAbundanceLS* function to create abundance maps for the end-members and choose the full restricted least square method (FRLS). The task uses the spatial dimensions as input data and returns the abundance charts as 3-D arrays. Every channel represents the end-members abundance map from the appropriate signature features. The input data in this work has spatial dimensions of 610 by 340 and nine end-members. As a result, the generated abundance map measures 610 by 340 by 9.

5. Results of developing satellite hyperspectral image processing

5. 1. Identifying the names of classes and visualizing their profiles

Visualization of the obtained Red-Green-Blue (RGB) image is shown in Fig. 2.

As mentioned earlier, the tested data includes an end-member signatures matrix that categorizes ground truth data into nine classes. A table for the names of classes of every end-member with its associated column for the signatures matrix is listed in Table 1, while the plotting of the end-member profiles is shown in Fig. 3.

Fig. 2. Visualization for the obtained Red-Green-Blue image

Table 1

End-members with their associated column in the signatures matrix

Column of sig	End-member category name
1	{'Shadows'}
2	{'Self-blocking bricks'}
3	{'Bitumen'}
4	{'Bare soil'}
5	{'Painted metal sheets'}
6	{'Trees'}
7	{'Gravel' }
8	{'Meadows'}
9	{'Asphalt'}

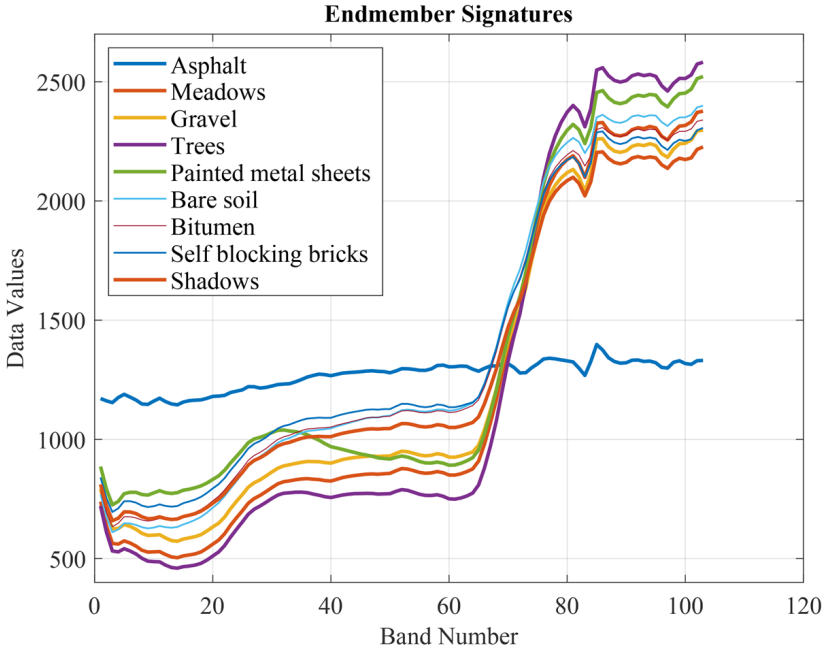

Fig. 3. Plotting of the end-member profiles

Therefore, every feature of sig contains the end-member a ground truth class signature.

5. 2. Estimating Abundance Maps

Visualization of the abundance maps is shown in Fig. 4.

These results estimate the abundance maps using the FRLS method for the end-member classes including Shadows, Self-blocking bricks, Bitumen, Bare soil, Painted metal sheets, Trees, Gravel, Meadows, and Asphalt.

5. 3. Performing Maximum Abundance Classification

An image of the color code with the highest abundance rate for the pixels classified is shown in Fig. 5, while Fig. 6 visualizes the application of Maximum Abundance Classification maps for Shadows, Self-blocking bricks, Bitumen, Bare soil, Painted metal sheets, Trees, Gravel, Meadows, and Asphalt end-member classes.

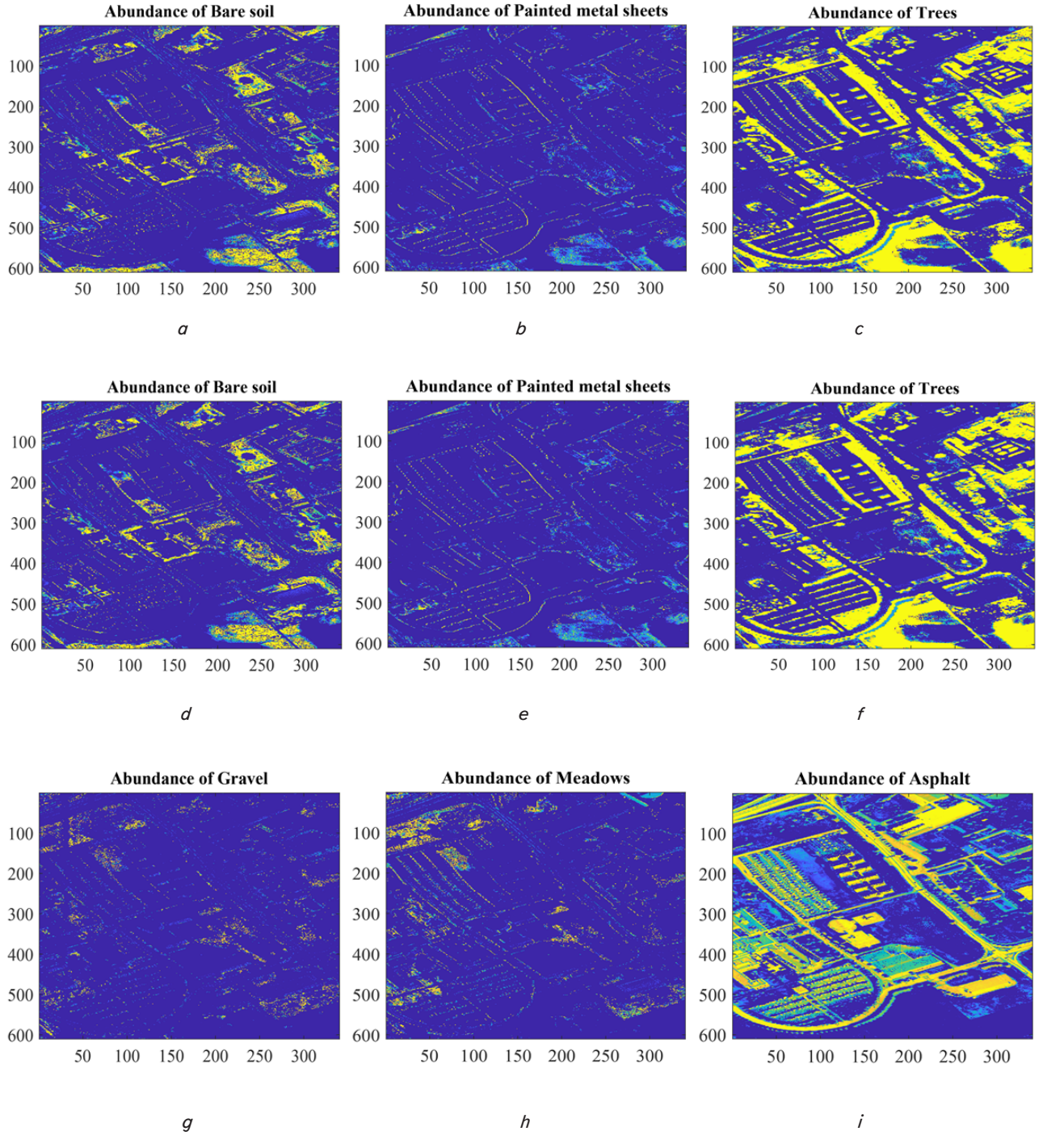

Fig. 4. Visualization of the abundance maps using the full restricted least square method, an abundance of: *a* – shadows; *b* – self-blocking bricks; *c* – bitumen; *d* – bare soil; *e* – painted metal sheets; *f* – trees; *g* – gravel; *h* – meadows; *i* – asphalt

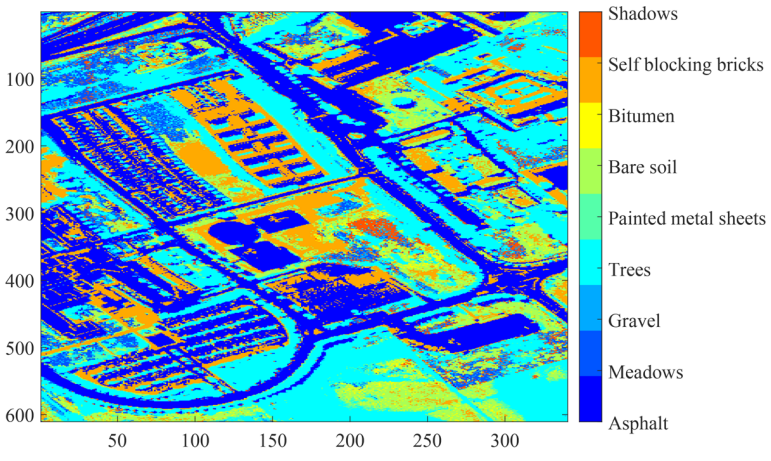

Fig. 5. An image of color code with the highest abundance rate for the pixels classified

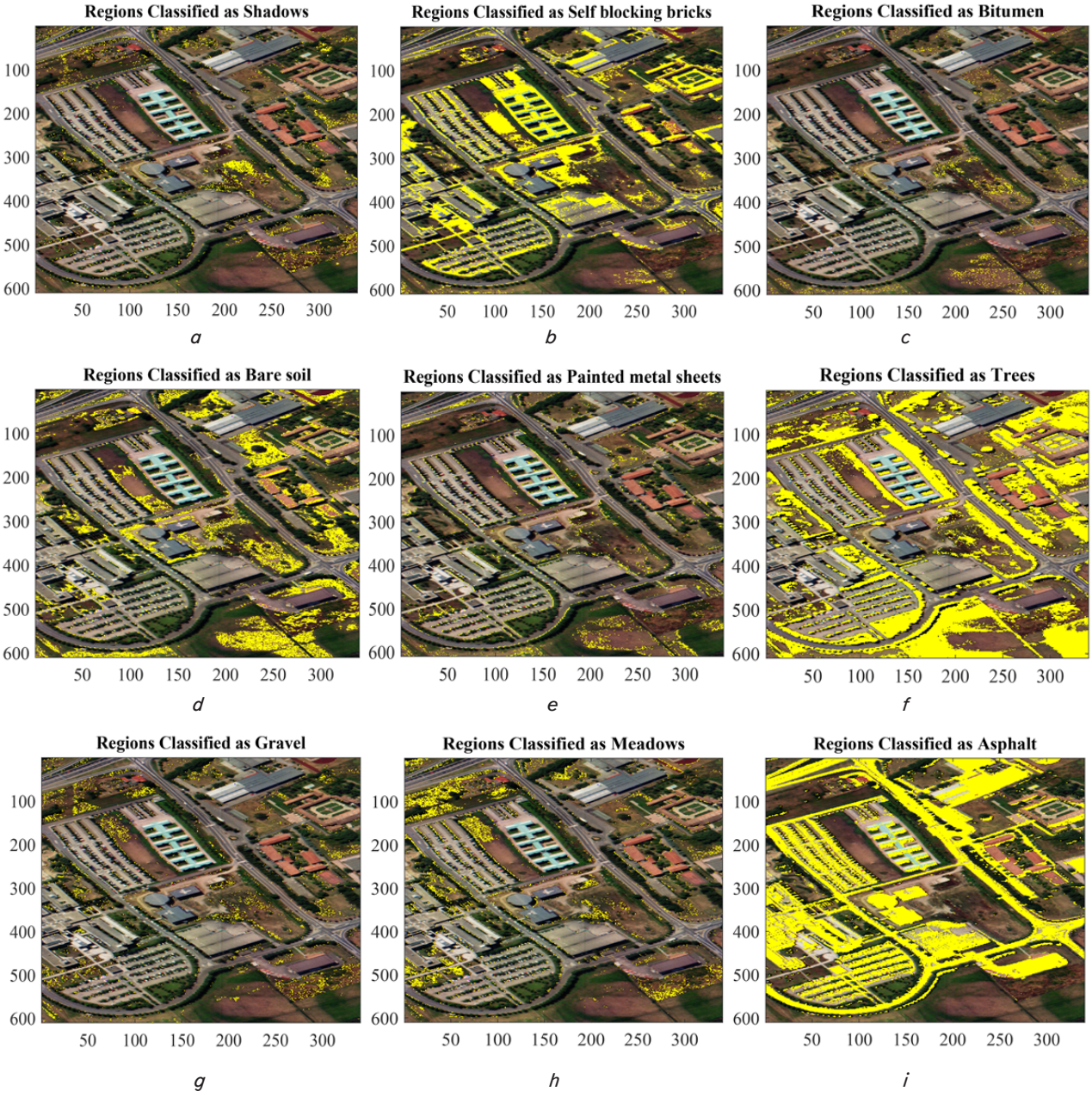

Fig. 6. Visualization of applying Maximum Abundance Classification maps for: *a* – shadows; *b* – self-blocking bricks; *c* – bitumen; *d* – bare soil; *e* – painted metal sheets; *f* – trees; *g* – gravel; *h* – meadows; *i* – asphalt

These figures show the overlaid hyperspectral images with classified areas over their associated class names that accurately classified the brick, asphalt, bare soil, and tree regions.

6. Discussion of the results of developing satellite hyperspectral image processing

An estimate for the hyperspectral data RGB image is shown in Fig. 1, where the contrast of this image has been improved using the central wavelengths and hyperspectral data cube. The tested data includes an end-member signatures matrix that categorizes ground truth data into nine classes. A table for the names of classes of every end-member with its associated column for the signatures matrix is listed in Table 1, while the plotting of the end-member profiles is shown in Fig. 2, where each end-member has its own profile. Fig. 3 visualized the results of estimating the abundance maps using the FRLS method for the end-member classes including Shadows, Self-blocking bricks, Bitumen, Bare soil, Painted metal sheets, Trees, Gravel, Meadows, and Asphalt. The function uses the spatial dimensions as input data and returns the 3-D array abundance maps. As a result, the generated abundance map measures 610 by 340 by 9. In contrast, the results of the overlaid hyperspectral image and classified areas over their associated class names show that the Maximum Abundance Classification can accurately classify the brick, asphalt, bare soil, and tree regions as shown in Fig. 5.

As a comparison with other techniques, the developed satellite hyperspectral image processing with maximum abundance classifier performs better with such images of 9-dimensional data when compared with the K-means clustering [15] and the spectral matching [16] that were applied for datasets with smaller end-members.

The use of a dataset from Pavia University with only nine end-member category names limits the applicability of the developed solutions. This will motivate us to test this technique on a wider range of end-members' applications.

The disadvantage of the proposed solution is the complexity of the classifier model, which is increased with the number of classes. This can be eliminated by expanding the application of this method over a more modern dataset with larger end-members in the future.

7. Conclusions

1. The obtained results of the tested data showed that nine end-members have been categorized and their associated profiles have been plotted. These profiles demonstrated that each end-member class has its own signature. All end-members with class signatures vary from about 700–2,500 during the change from 60 to 80 in band number.

2. The developed model generated abundance maps for the end-members using the full constrained least squares (FRLS) method with relative accuracy and the created abundance map measures 610 by 340 by 9.

3. The visualization of the overlaid hyperspectral image and classified areas over their associated class names show that the Maximum Abundance Classification can classify five regions accurately including the brick, asphalt, bare soil, and tree.

Conflict of interest

The authors declare that they have no conflict of interest in relation to this research, whether financial, personal, authorship, or otherwise, that could affect the research and its results presented in this paper.

Financing

The study was performed without financial support.

Data availability

The manuscript has associated data in the data repository.

Acknowledgments

The authors would like to express their deepest gratitude to the Department of Clinical Laboratory Sciences, College of Pharmacy, University of Mosul-Iraq for their support to complete this research.

References

1. Sarić, R., Nguyen, V. D., Burge, T., Berkowitz, O., Trtílek, M., Whelan, J. et al. (2022). Applications of hyperspectral imaging in plant phenotyping. Trends in Plant Science, 27 (3), 301–315. doi: https://doi.org/10.1016/j.tplants.2021.12.003
2. Sugawara, S., Sugizaki, S., Nakayama, Y., Taniguchi, H., Ishimaru, I. (2021). Preliminary study for detection of adhesive on a painted ceramic plate and varnish on printed paper using near-infrared hyperspectral imaging at wavelengths of 1.0–2.35 μm. Infrared Physics & Technology, 117, 103809. doi: https://doi.org/10.1016/j.infrared.2021.103809
3. Xue, Q., Qi, M., Li, Z., Yang, B., Li, W., Wang, F., Li, Q. (2021). Fluorescence hyperspectral imaging system for analysis and visualization of oil sample composition and thickness. Applied Optics, 60 (27), 8349. doi: https://doi.org/10.1364/ao.432851
4. Shijer, S. S., Sabry, A. H. (2021). Analysis of performance parameters for wireless network using switching multiple access control method. Eastern-European Journal of Enterprise Technologies, 4 (9 (112)), 6–14. doi: https://doi.org/10.15587/1729-4061.2021.238457
5. Mohammed, A. B., Al-Mafrji, A. A. M., Yassen, M. S., Sabry, A. H. (2022). Developing plastic recycling classifier by deep learning and directed acyclic graph residual network. Eastern-European Journal of Enterprise Technologies, 2 (10 (116)), 42–49. doi: https://doi.org/10.15587/1729-4061.2022.254285
6. Guda, M., Gasser, S., El-Mahallawy, M. S., Shehata, K. (2020). FPGA Implementation of L1/2 Sparsity Constrained Nonnegative Matrix Factorization Algorithm for Remotely Sensed Hyperspectral Image Analysis. IEEE Access, 8, 12069–12083. doi: https://doi.org/10.1109/access.2020.2966044

7. Gao, L., Zhang, B., Sun, X., Li, S., Du, Q., Wu, C. (2013). Optimized maximum noise fraction for dimensionality reduction of Chinese HJ-1A hyperspectral data. EURASIP Journal on Advances in Signal Processing, 2013 (1). doi: https://doi.org/10.1186/1687-6180-2013-65
8. Lv, N., Han, Z., Chen, C., Feng, Y., Su, T., Goudos, S., Wan, S. (2021). Encoding Spectral-Spatial Features for Hyperspectral Image Classification in the Satellite Internet of Things System. Remote Sensing, 13 (18), 3561. doi: https://doi.org/10.3390/rs13183561
9. Iyer, P., A, S., Lal, S. (2021). Deep learning ensemble method for classification of satellite hyperspectral images. Remote Sensing Applications: Society and Environment, 23, 100580. doi: https://doi.org/10.1016/j.rsase.2021.100580
10. Hagag, A., Fan, X., Abd El-Samie, F. E. (2017). HyperCast: Hyperspectral satellite image broadcasting with band ordering optimization. Journal of Visual Communication and Image Representation, 42, 14–27. doi: https://doi.org/10.1016/j.jvcir.2016.11.006
11. Arellano, P., Tansey, K., Balzter, H., Boyd, D. S. (2015). Detecting the effects of hydrocarbon pollution in the Amazon forest using hyperspectral satellite images. Environmental Pollution, 205, 225–239. doi: https://doi.org/10.1016/j.envpol.2015.05.041
12. Shin, J., Kim, K., Ryu, J.-H. (2020). Comparative study on hyperspectral and satellite image for the estimation of chlorophyll a concentration on coastal areas. Korean Journal of Remote Sensing, 36 (2_2), 309–323. doi: https://doi.org/10.7780/kjrs.2020.36.2.2.7
13. Yang, M.-D., Huang, K.-H., Tsai, H.-P. (2020). Integrating MNF and HHT Transformations into Artificial Neural Networks for Hyperspectral Image Classification. Remote Sensing, 12 (14), 2327. doi: https://doi.org/10.3390/rs12142327
14. Huang, H., Chen, M., Duan, Y. (2019). Dimensionality Reduction of Hyperspectral Image Using Spatial-Spectral Regularized Sparse Hypergraph Embedding. Remote Sensing, 11 (9), 1039. doi: https://doi.org/10.3390/rs11091039
15. Veligandan, S. K., Rengasari, N. (2018). Hyperspectral image segmentation based on enhanced estimation of centroid with fast K-means. The International Arab Journal of Information Technology, 15 (5), 904–911. Available at: https://iajit.org/portal/PDF/September%202018,%20No.%205/10400.pdf
16. Lin, L., Chen, C., Xu, T. (2020). Spatial-spectral hyperspectral image classification based on information measurement and CNN. EURASIP Journal on Wireless Communications and Networking, 2020 (1). doi: https://doi.org/10.1186/s13638-020-01666-9